ORIGINAL ARTICLE

Hydrogen Embrittlement Characteristics of Low Carbon Steels After Heat and Surface Treatments

**Mitsuhiro Okayasu[1] · Takehiro Kokado[1]**

Abstract The hydrogen embrittlement (HE) characteristics of the low carbon steels: Fe-xC-1.5Mn-0.03Si (0.05C, 0.1C, and 0.15C) with ultimate tensile strength (UTS) of ~1200 MPa, were examined experimentally after heating and surface treatment processes. For this investigation, the low carbon steels with different microstructural characteristics, including phase structures, precipitates, and internal strain, were employed. The high internal strain was seen in the Fe-0.15C steels after cold rolling (CR), water quenching (WQ), and bake hardening (BH) process, while the low strain was obtained in the steel samples after the annealing process. The high strain for CR and WQ (and BH) is caused by severe plastic deformation and the phase transformation of the martensite structure, respectively. Carbide particles were precipitated in the WQ and BH samples, and the amount of carbide was correlated with their carbon content. HE occurred only in the CR-0.15C and WQ-0.15C samples although the low UTS of ~1200 MPa was used, where the fracture strain decreased significantly. HE was attributed to the high internal strain and high carbon content which led to the hydrogen trapping site. A multiple regression analysis was also carried out to estimate the extent of HE of the low carbon steels.

Keywords Low carbon steel · Hydrogen embrittlement · Fracture strain · Carbide precipitate · Surface treatment

✉ Mitsuhiro Okayasu
  mitsuhiro.okayasu@utoronto.ca

1 Department of Mechanical and Systems Engineering, Okayama University, 3-1-1 Tsushimanaka, Kita-Ku, Okayama 700-8530, Japan

1 Introduction

There has recently been a great demand for high strengthening of carbon steel for construction equipment and industrial machinery. In particular, high-strength martensitic steels have been used in various applications, such as automobiles, constructions, and tools [1]. In recent years, low carbon sheet steels quenched to martensite have been used for various automotive parts that need high mechanical properties for crash protection in side-impact and rollover accidents. However, it is required to consider that high-strength martensitic steels are sensitive to HE [1]. Namely, HE of the related steels deteriorates with an increase in tensile strength exceeding 1200 MPa. Several studies have been reported on the information of the resistance to HE in low carbon steels with as low as UTS 1200 MPa [2, 3]. In this case, a small amount of hydrogen (sub mass ppm) makes the embrittlement of the steels. There are several possibilities to make HE [4]: the hydrogen element enhances grain boundary decohesion (HEGBDE), the hydrogen-enhanced localized plasticity (HELP), and the hydrogen-enhanced strain-induced vacancy (HESIV).

The hydrogen can initially be present either externally or internally in the steels, in which the steel surfaces could be chemically reacted with the following reaction as contact with an aqueous environment [5]:

$$xFe + yH_2O \rightarrow Fe_xO_y + 2yH^+ \tag{1}$$

$$H^+ + e \rightarrow H_{(ads)} \tag{1a}$$
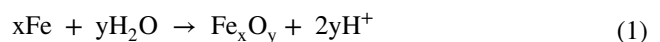
The adsorbed hydrogen ($H_{(ads)}$) migrates into the metal matrix causing metal–hydrogen interaction, which can be introduced during the steelmaking process, heat treatment, surface treatment, or service [5]. The difference in HE is

caused by the hydrogen trap state at and/or around the plastically strained interfaces between the matrix and cementite [3]. Hydrogen embrittlement of hardened low carbon steel has been investigated, where the steel specimens, tempered at 460 °C and 520 °C, showed little sensitivity to HE, and the reduction of sensitivity to hydrogen-induced fracture is caused by decrement of dislocations and cementite particles [6]. Moreover, the role of hydrogen in the plastic strain of the low carbon steel was investigated in the yielding and linear strain hardening stage [7]. It is also considered that HE is attributed to the surface condition of the carbon steel, because of the change of the extent of hydrogen penetration [8].

Although many scientists have examined HE of the low carbon steels, there seems to be still a lack of information concerning the HE characteristics of the low strength and low carbon steels. Hence, in the present work, an attempt was made to investigate the HE characteristics of low carbon steels with different internal strains, microstructural formation, and surface conditions.

2 Experimental Procedures

2.1 Materials and Specimens

In this study, Fe-xC-1.5Mn-0.3Si-0.4Mo steels formed via hot rolling were used (0.05C, 0.1C, or 0.15C). Table 1 indicates the chemical compositions of the three carbon steels. Figure 1a shows the heating processes for the sample preparation. The test samples were made by different processes, including cold rolling (CR), water quenching (WQ), quenching and tempering (BH), and quenching and annealing (AN). The CR sample was manufactured with a thickness of 1.0 mm using a hot-rolled sheet. The WQ process was performed in cold water after heating above the A_3 line (i.e., 800 °C) for a few minutes, and the BH

Table 1 Chemical compositions of Fe-xC-1.5Mn-0.03Si steels (mass%)

	C	Mn	Si	P	S	Ti	Al	Cr	N
Fe-0.05C	0.047	1.53	0.03	0.018	0.002	0.002	0.03	0.005	0.002
Fe-0.1C	0.098	1.52	0.02	0.018	0.002	0.002	0.03	0.005	0.002
Fe-0.15C	0.150	1.51	0.02	0.018	0.002	0.002	0.03	0.005	0.002

Fig. 1 **a** Schematic diagram showing the sample preparation processes of the low carbon steels for the cold rolling (CR), water quenching (WQ), quenching and tempering (BH), and annealing (AN). **b** Schematic diagram showing the nitriding processes of the low carbon steels for the cold rolling (CR)
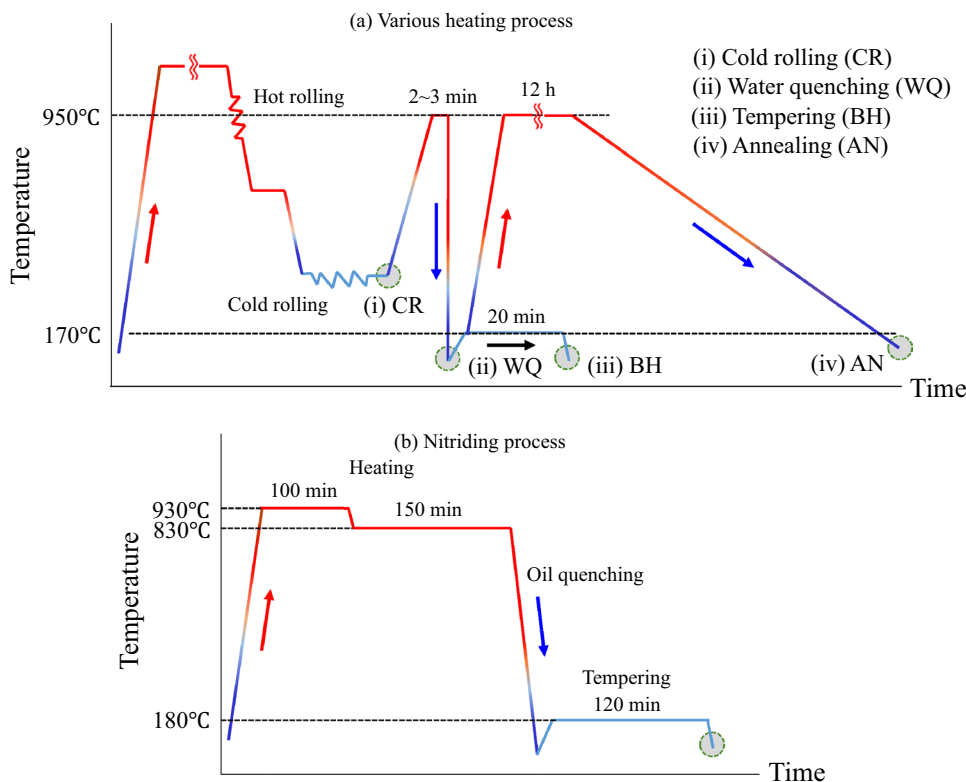
process was conducted using the WQ sample by tempering at 170 °C for 20 min. The AN process was performed using WQ by heating to 950 °C for 12 h before air cooling.

2.2 Surface Treatments

To examine the effect of the surface condition on the extent of hydrogen embrittlement characteristics, two different surface treatments were carried out: nitriding and shot-peening processes. Figure 1b shows the schematic illustration of the nitriding process. The nitriding was conducted by the following process: the sample was heated to 930 °C for 100 min before heating to 830 °C for 150 min. The heated sample was quenched into oil before heating to 180 °C for 120 min. On the other hand, the shot-peening was executed for 3 min using steel peening media with 0.4 mm and 1.2 mm in diameter, where the shot force was about 17.8 N·min^{-1}.

2.3 Hydrogen Charging

The HE characteristics of the steel samples were examined after hydrogen charging using an ammonium thiocyanate (NH$_4$SCN) solution. The hydrogen content in the steel samples was measured by thermal desorption analysis using a gas chromatograph with a linear heating rate of 3.3 °C min^{-1} from 25 to 400 °C. The amount of hydrogen gas was measured with a 5-min interval using argon as a carrier gas.

2.4 Microstructural Analysis

The microstructure of the steel samples was observed using an electron backscatter diffraction (EBSD) analysis and scanning transmission electron microscopy (STEM). EBSD analysis was executed with a beam current 12 mA, an accelerating voltage 15 kV, and a step size 1 μm. On the other hand, STEM analysis was performed to examine the precipitation characteristics of the steels using a replica sample made via mechanical thinning followed by electrolytic polishing with 10% perchloric acid and 90% ethanol.

2.5 Mechanical Testing

The HE characteristics were evaluated by the change of the tensile properties, e.g., ultimate tensile strength and strain to failure, where the test specimens with and without hydrogen were employed. In this approach, tensile test was carried out using the dumbbell shaped specimen after the hydrogen charging. Figure 2 shows the photographs of the test specimens after the shot-peening and nitriding processes. It should be noted that the shot-peened specimens were fixed to the testing machine using pins due to the high
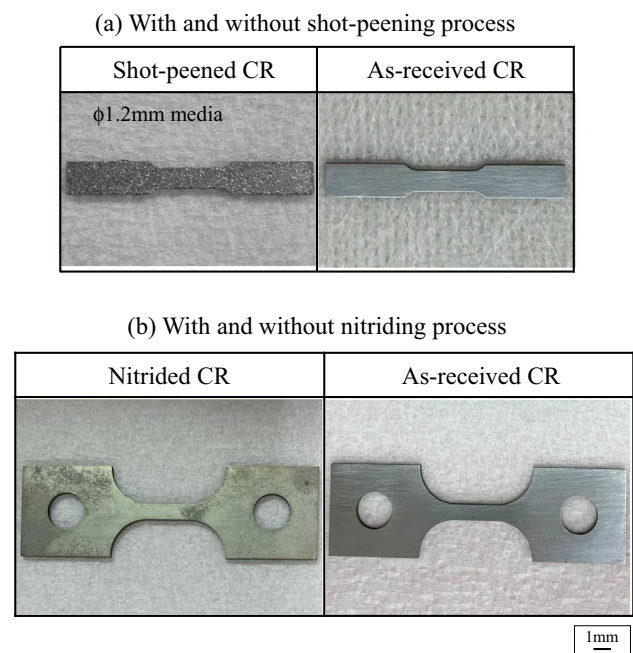

Fig. 2 Photographs of CR sample with and without surface treatment: **a** shot-peening process and **b** nitriding process

hardness of the specimen surface. The tensile tests were conducted using a screw-driven universal testing machine with a 50 kN capacity, in which the test specimens were loaded at 0.1 mm min^{-1} and 1 mm min^{-1} via stroke control until the specimen was completely fractured. The specimens were designed with a rectangular dumbbell shape of 20 mm × 10 mm × 1 mm.

3 Results

3.1 Microstructural Characteristics

Figure 3a shows the microstructural characteristics of the three carbon steels after different treatments, showing the image quality (IQ), crystal orientation (IPF: inverse pole figure), and internal strain (KAM: Kernel average misorientation). It is clear that different microstructural formation is seen depending on the sample, whereas no clear change of microstructure is observed even if the carbon content is altered. For all CR samples, severely deformed microstructure is observed. After the annealing process (AN), the internal strain is reduced and ferrite phases are apparently detected. For the WQ samples, high internal strain in lath martensite was seen which is similar to that for CR. Such martensite and high strain is also observed in the BH samples.

Figure 3b displays the results of EBSD analysis of the shot-peened and nitrided sample. Note that the
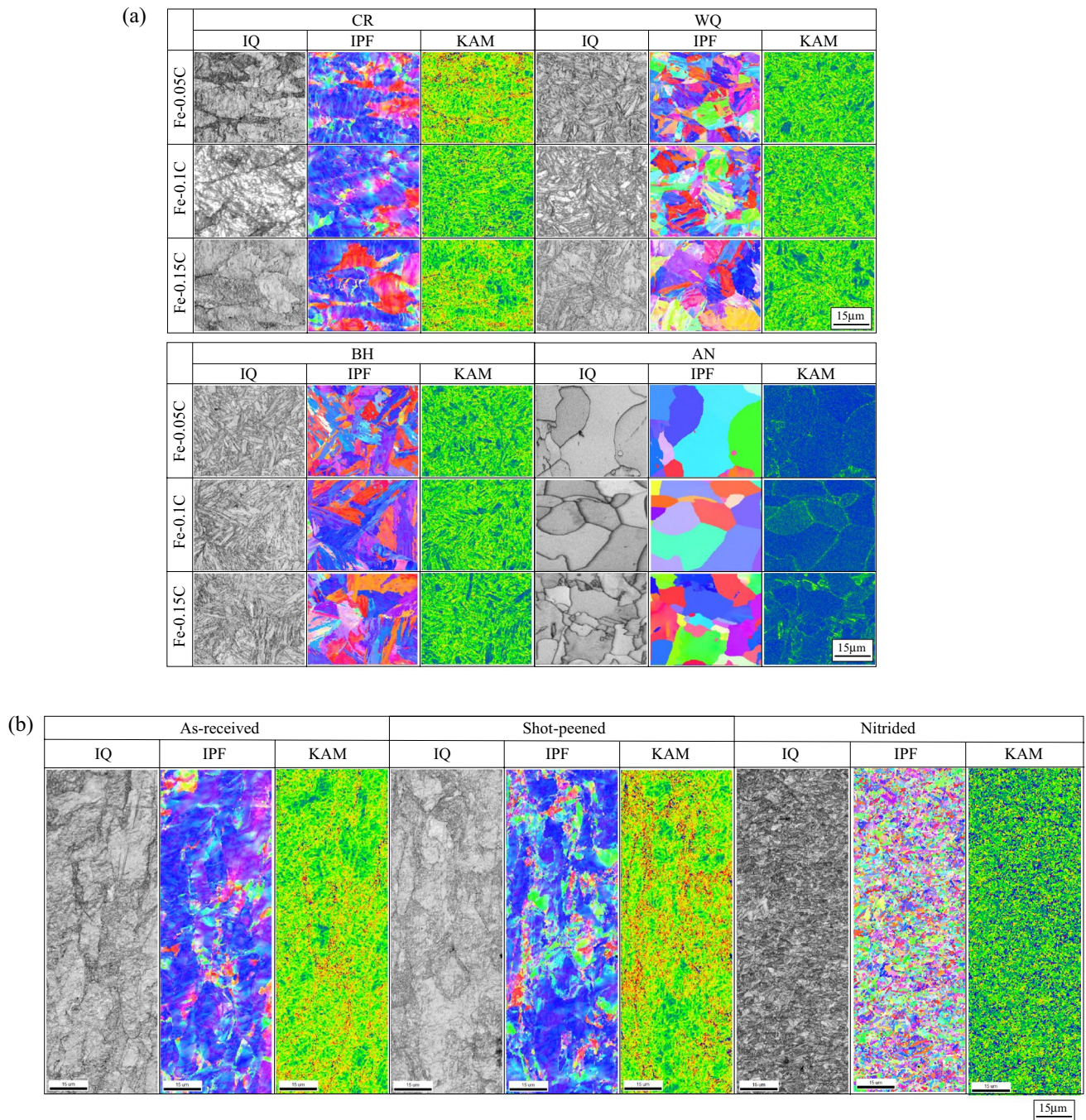
(a)

(b)

Fig. 3 a EBSD analyses of the low carbon steels showing the image quality, inverse pole figure, and Kernel average misorientation: CR, WQ, BH, and AN samples. **b** EBSD analyses of the low carbon steels showing the image quality, inverse pole figure, and Kernel average misorientation: as-received, shot-peened, and nitrided samples

microstructures were observed near the sample surface, and the shot-peening process was conducted using φ1.2 mm media. With the comparison of the as-received sample, the KAM value increases overall for the shot-peened sample. On the other hand, the crystal orientation of the nitrided sample was fine and scattered although the KAM value decreased

clearly. The reduction of the KAM value may be attributed to the low internal strain arising from the heating process.

Figure 4a shows the Vickers hardness of the three carbon steels prepared by the CR, AN, WQ, and BH processes. Even though there is no clear effect of carbon content on the microstructure, the hardness value has altered, e.g., the higher the carbon content, the higher the hardness. The

Fig. 4 **a** Vickers hardness of the Fe-xC steels: CR, WQ, BH, and AN samples. **b** Vickers hardness of the CR-Fe-0.15C after: nitriding and shot-peening process
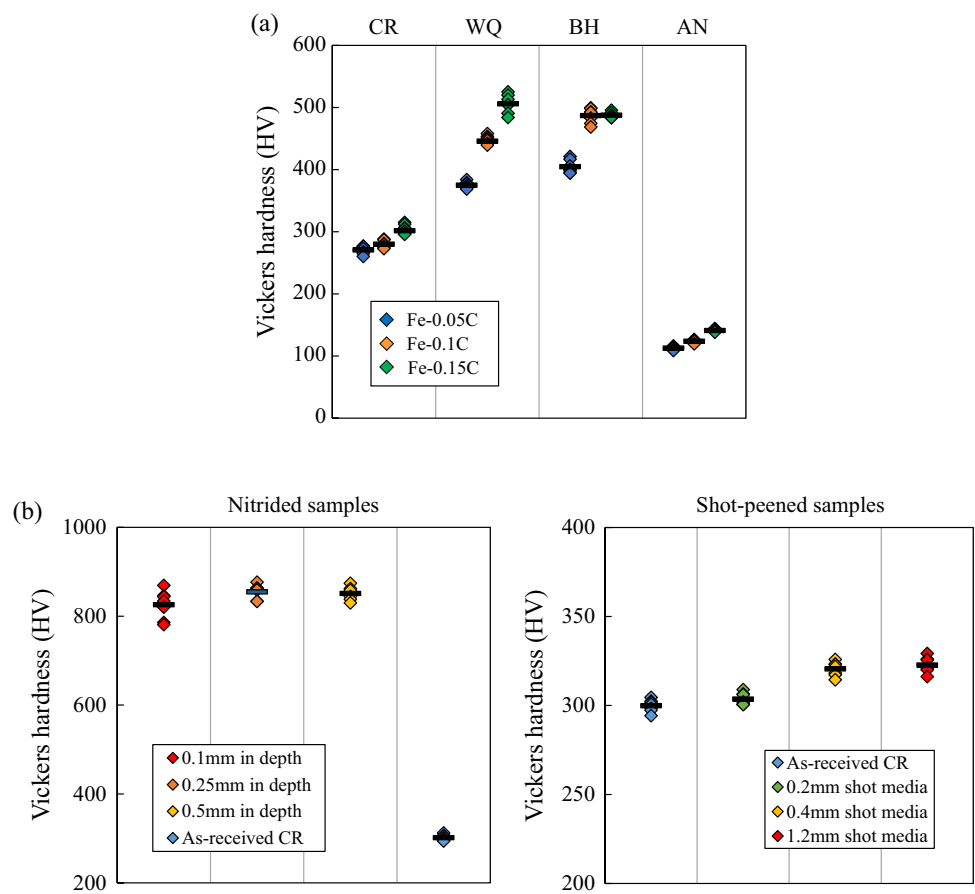
hardness of CR samples was higher and lower than that for AN and WQ (and BH), respectively. The high hardness of CR and WQ could be caused by the high internal strain as observed by the EBSD analysis. The hardness values of BH are relatively similar to those for WQ.

Figure 4b shows the Vickers hardness of the shot-peened and nitrided samples, observed at a different depth from the surface (0.1, 0.25, and 0.5 mm) for nitrided sample and 0.5 mm for the shot-peened sample. It is clear that the hardness level increases about three times with the nitriding process. It should be noted that the high hardness value for the nitrided sample is observed in the entire area of the sample. On the other hand, a slight increment of the hardness is obtained with the shot-peening process, in which the hardness for the sample after shot-peened with 1.2 mm media is enhanced by about 10%.

3.2 Hydrogen Embrittlement Characteristics

Figure 5a shows the tensile stress–tensile strain curves (*S*–*S*) of the three carbon steels (CR, AN, WQ, and BH) before and after the hydrogen charging, and the obtained ultimate tensile strength and fracture strain are summarized in Fig. 5b. It is clear first that the UTS values of our low carbon steels

are lower than 1200 MPa, although their UTS is altered depending on the sample. The material properties of the related carbon steels with the low UTS may not be affected by hydrogen. The change of UTS for the sample is overall similar trend to the results of the hardness: (i) the higher the carbon content, the higher the UTS, and (ii) the higher and lower UTS for WQ (and BH) and AN, respectively. The opposite trend is detected for their fracture strain: (i) the lower the fracture strain, the higher the carbon content, and (ii) the higher ductility for AN.

On hydrogen charging, their tensile properties were altered, due to the different extent of HE. Although the UTS values were not changed for all samples, the fracture strain (ε_f) decreases significantly for the CR and WQ samples, in particular, the samples with high carbon content with 0.15C make severe HE, e.g., the CR samples. In contrast, HE is recovered by BH and AN, where no clear reduction of UTS is observed. Namely, hydrogen has little effect on the tensile strength, while significantly reduces the ductility [9]. On the other hand, the ε_f value did not change clearly for all other samples. From this result, it can be described first that (i) HE occurs even if the UTS is less than 1200 MPa; and (ii) the high carbon content and high plastic strain affect HE.
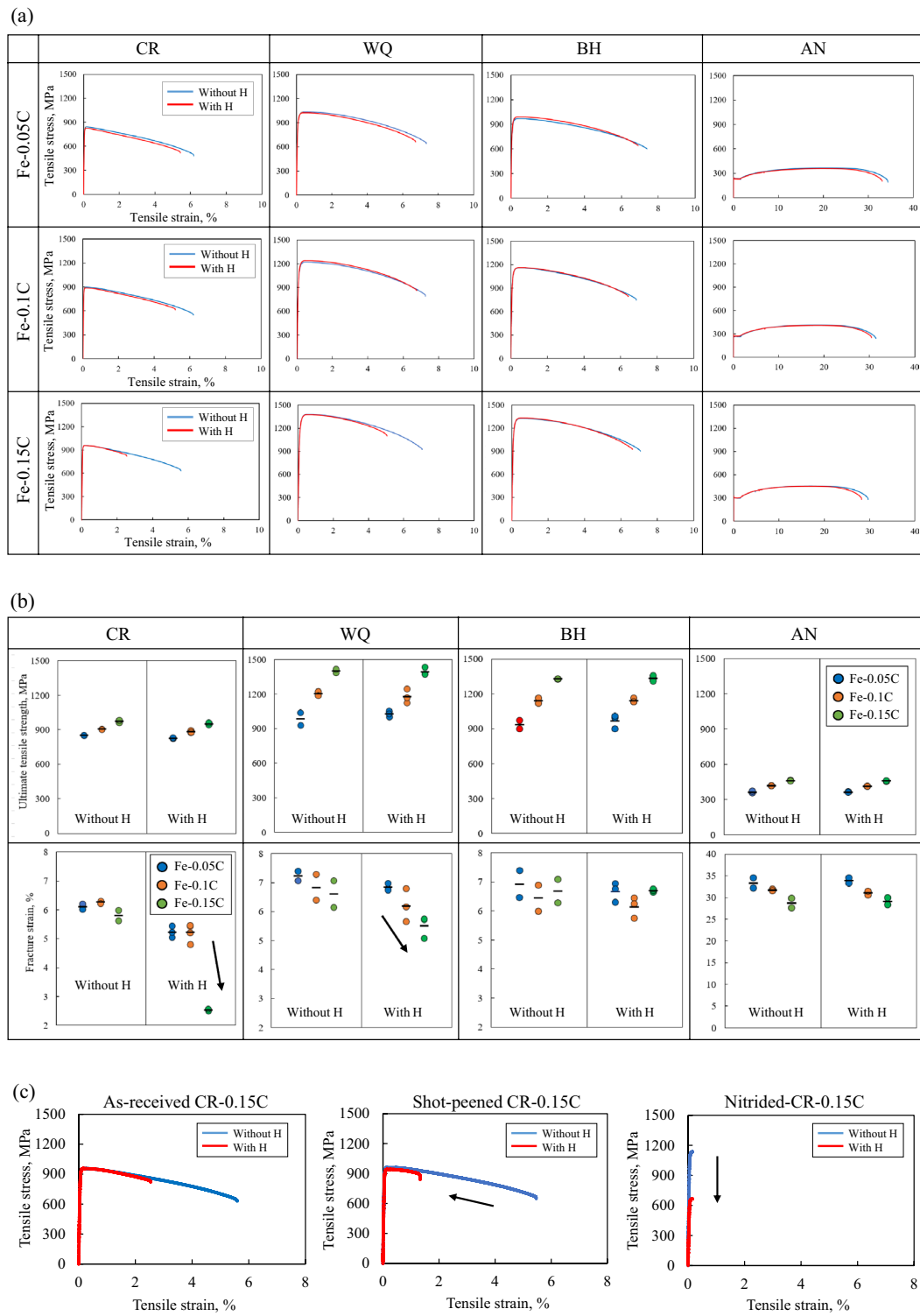
(a)

(b)

(c)

Fig. 5 **a** Tensile stress versus tensile strain for the low carbon steels with and without hydrogen charging (CR, WQ, BH, and AN). **b** Ultimate tensile strength (σ_{UTS}) and fracture strain (ε_f) results for the low carbon steels with and without hydrogen charging (CR, WQ, BH, and AN), **c** Tensile stress versus tensile strain for the low carbon steels with and without hydrogen charging (shot-peened and nitrided CR-0.15C sample)

Figure 5c displays *S–S* curves of the surface-treated Fe-0.15C steels (shot-peened and nitrided samples) before and after the hydrogen charging. As seen in the results of the shot-peened samples, HE occurred severely compared to that before the shot-peening process, where the fracture strain for the shot-peened sample is about 1%, which is more than half of that before hydrogen charging. This occurrence might be affected by the high internal strain or high dislocation density, i.e., the HELP mechanism, which is related to the high KAM values shown in Fig. 3b. One the other hand, tensile strength of the CR-0.15C sample increases with the nitriding process, while the fracture strain dropped significantly. With the hydrogen charging, the tensile strength of the nitrided sample decreases, which is about half of that without hydrogen charging. Such reduction of the tensile strength would also be affected by the hydrogen embrittlement due to the hydrogen trap site in the boundary of the microstructures, see Fig. 3b.

To understand the hydrogen embrittlement properties of the three carbon steel samples after several treatments in detail, the amount of hydrogen was measured. Figure 6 displays variation in the cumulative hydrogen content with sample heating temperature released for (a) the CR, WQ, BH, and AN samples and b shot-peened and nitrided samples after 48 h of hydrogen charging using NH_4SCN solution. As seen in Fig. 6a, a high amount of hydrogen was seen for the CR sample, and a low amount of hydrogen was detected for WQ. On the other hand, no clear hydrogen was observed in the BH and AN samples. In this case, hydrogen, released from the samples upon heating to approximately 120 °C, is considered to be the diffusible hydrogen content, which could make severe HE. In addition, the samples with the high carbon content accumulate a high hydrogen amount. In this case, the higher-carbon alloys in the pearlitic phase could be attributed to the hydrogen trapping site [9]. From this result, the amount of hydrogen detected in the CR and WQ samples is related to their HE.

It is also clear from Fig. 6b that a large amount of hydrogen was obtained for the shot-peened and the nitrided samples compared to that for WQ, whereas their hydrogen amounts were lower than that for CR samples. It is interesting to mention that the diffusible hydrogen released from the shot-peened and the nitrided samples upon heating to about 125 °C and 150 °C, respectively, is slightly shifted to the high-temperature side. This occurrence may be related to the high resistance of the hydrogen diffusibility due to the high peened strain and complicated microstructure.

3.3 Fractography

To understand HE characteristics of our samples, fracture surface observation after the tensile tests was carried out using SEM. Figure 7a shows the SEM image of the fracture surface of the CR-0.15C, WQ-0.15C, and BH-0.15C samples with and without the hydrogen charging. It is clear that severe plastic deformation of necking was seen for all samples without hydrogen. However, brittle failure mode was detected for the CR-0.15C and WQ-0.15C samples with the hydrogen charging, where no or weak necking and cleavage or intergranular-like failure occurs. In this case, failure along the cementite and lath martensite might have occurred in CR and WQ, respectively. It is also clear in Fig. 7a that aluminum oxide (Al_2O_3) is detected on the fracture surface of the WQ-0.15 sample with hydrogen, which seems to the inclusions triggering brittle fracture. In this case, the crack initiation and propagation occurs from a cavity forming through debonding along the Al_2O_3 particle/matrix interface due to the hydrogen trapping in the interface [10].

Figure 7b displays the fracture surfaces of the surface-treated CR-0.15C samples with and without the hydrogen charging. It is clear that dimple base ductile failure is seen for the shot-peened sample before the hydrogen charging, while brittle intergranular failure is seen for the nitrided one. After the hydrogen charging, brittle failure mode is obtained in several regions in the shot-peened sample, where cleavage-like failure is detected. On the other hand, after the hydrogen charging, brittle-like failure with a dark color is seen which could make an acceleration of the failure during the tensile loading.

4 Discussion

To interpret the different extent of HE in the WQ and BH samples, the microstructural characteristics of WQ-0.05C, WQ-0.15C, and BH-0.15C were analyzed by STEM. Figure 8 shows STEM images of the WQ-0.05C, WQ-0.15C, and BH-0.15C samples. Similar to the EBSD analysis shown in Fig. 3, lath martensite structures are observed for the three samples. Carbon base precipitate (ε-carbide) with 100 nm in diameter is observed randomly in the martensite structures. As seen, the precipitate size and quantity in the WQ-0.15C sample is similar to those in the BH-0.15C sample, although low amount of the precipitates is visible in the WQ-0.05C sample, which is due to the different carbon content. However, there is no clear change of the microstructural characteristics between WQ- and BH-0.15C from the STEM analysis, although a different extent of HE was detected. The reason for this is not clear at the moment. In this case, BH makes the change of microstructural characteristics [11]: (i) interstitial solute atoms (carbon and nitrogen) migrate to the dislocations, and (ii) ε-carbide forms preferentially on dislocations. Those occurrences may affect the change of the severity of HE. Namely, dislocations cannot carry hydrogen
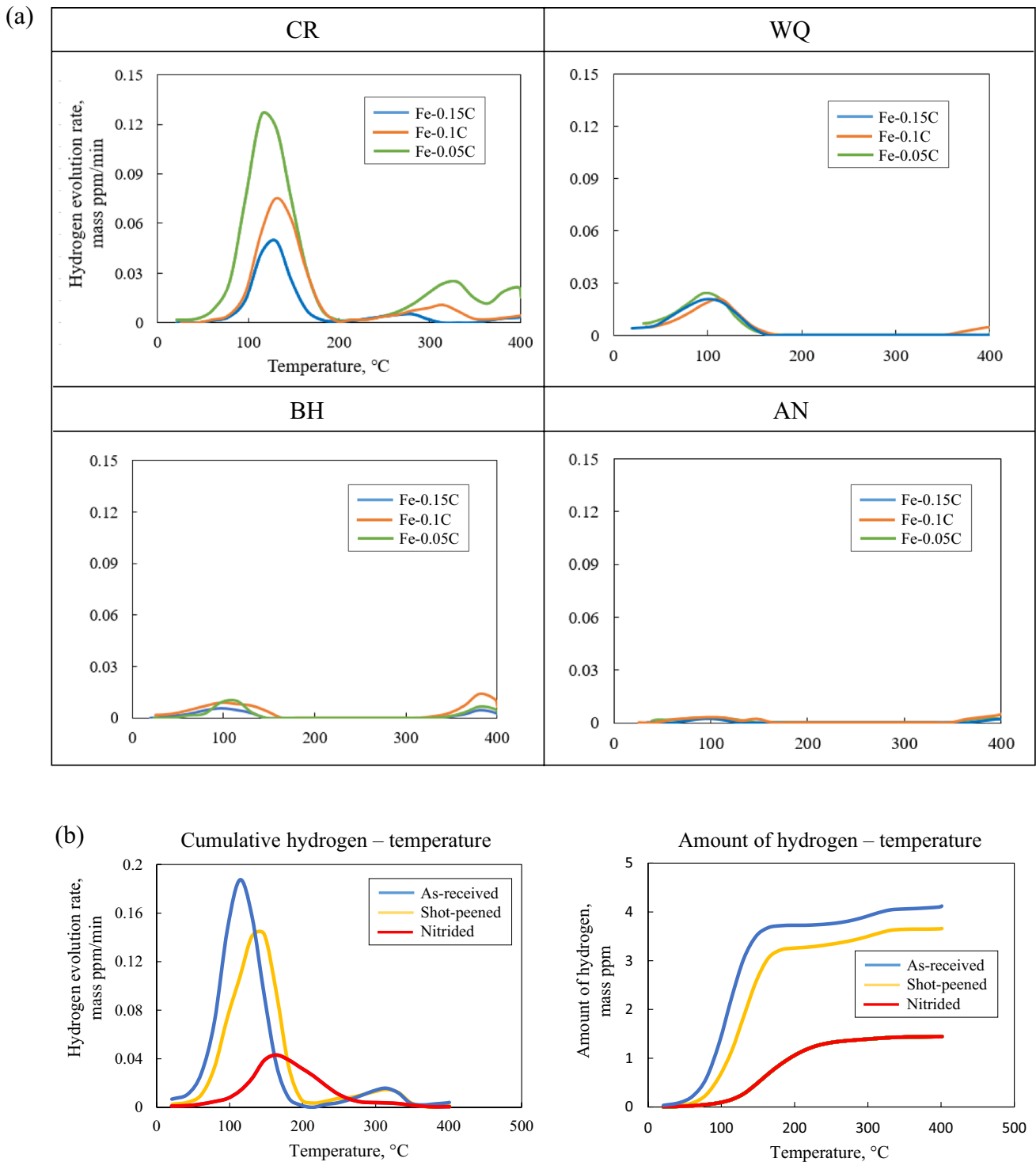
(a)

(b)

Fig. 6 **a** Variation in the cumulative hydrogen content with temperature for the low carbon steels (CR, WQ, BH, and AN) after hydrogen charging. **b** Variation in the cumulative hydrogen and amount of H atoms to the grain boundary, but details of this will be further examined in the future.

content with temperature for the CR-0.15C (as-received, shot-peened, and nitrided) after hydrogen charging

atoms to the grain boundary, but details of this will be further examined in the future.

To estimate the extent of hydrogen embrittlement accurately, a multiple regression analysis was conducted for the determination of the fracture strain using the obtained
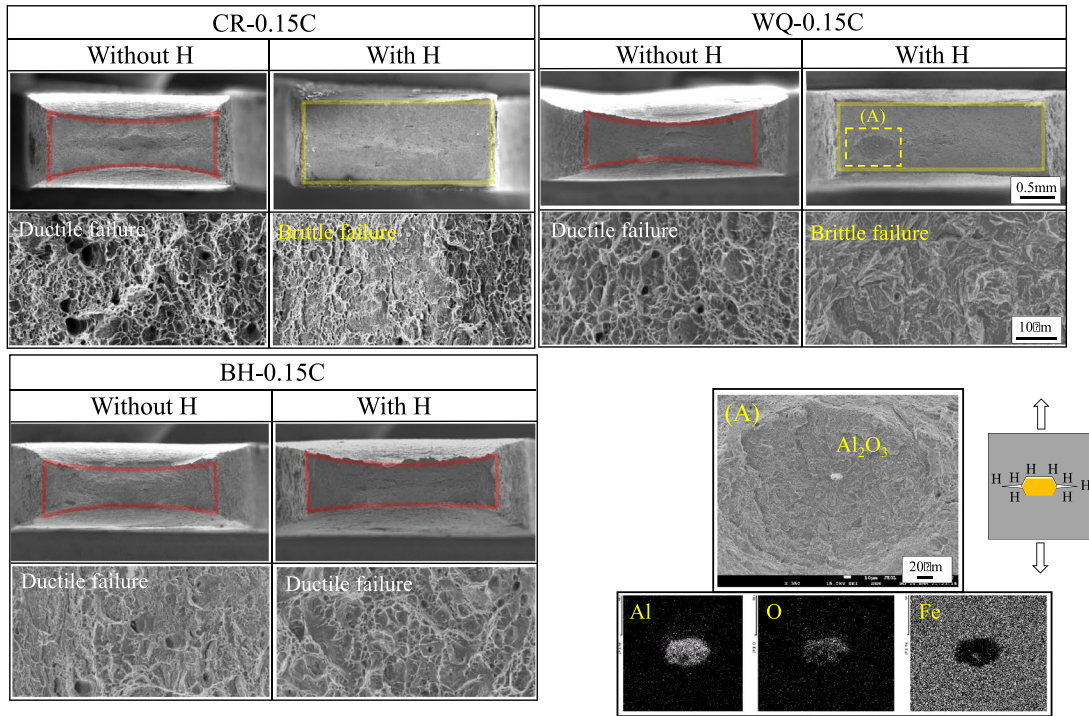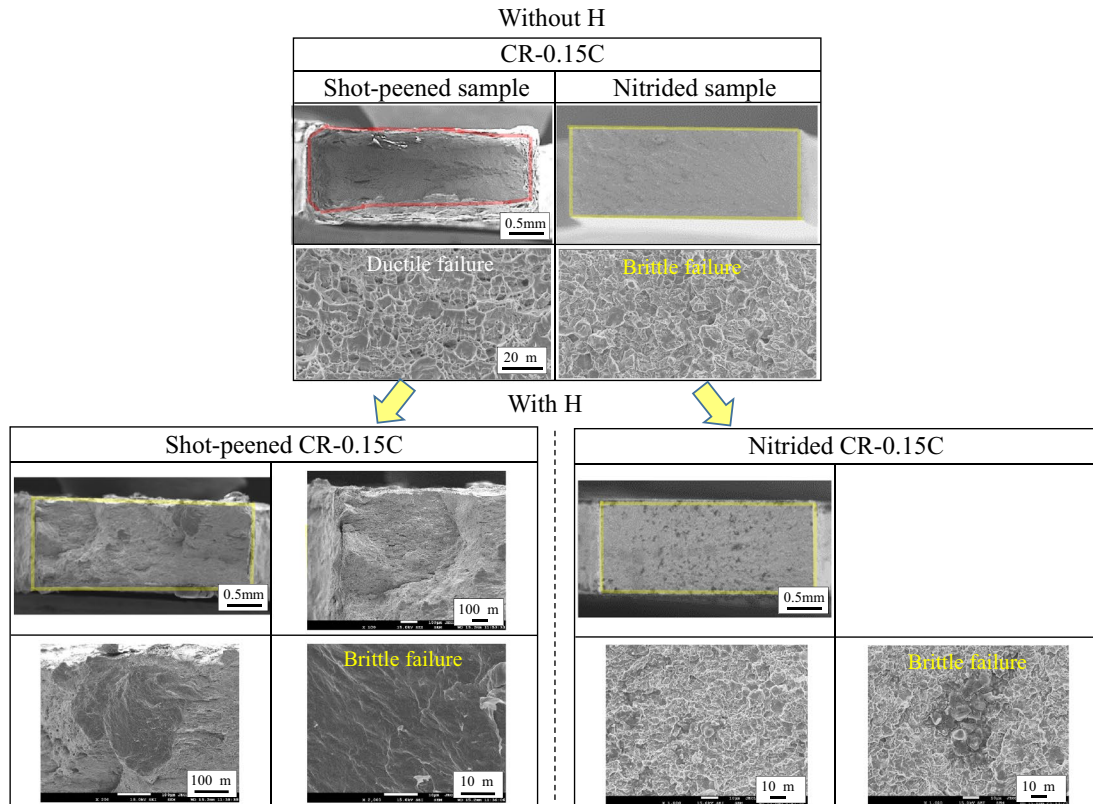
Fig. 7 **a** SEM images of the Fe-0.15C steel fracture surfaces: CR samples with and without hydrogen charging, **b** SEM images of fracture surfaces after tensile test for the Fe-0.15C steel with shot-peening and nitriding process
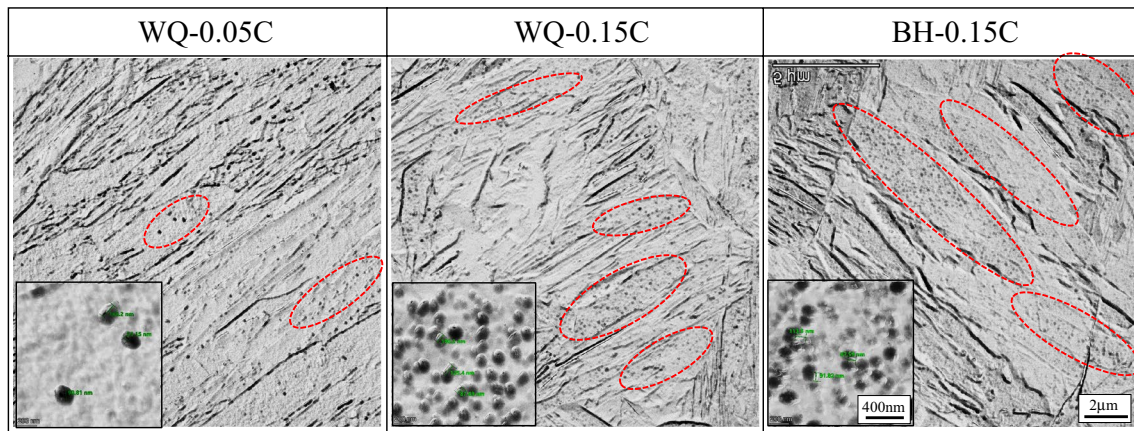
Fig. 8 STEM images of the WQ-0.05C, WQ-0.15C, and BH-0.15C steels showing carbide precipitates
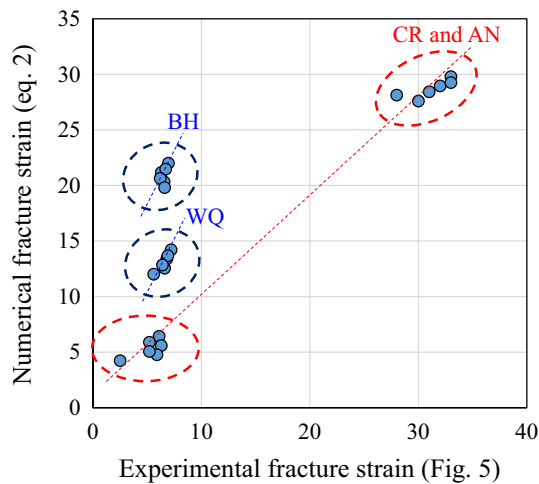

Fig. 9 Relationship between experimental fracture strain and numerical fracture strain

tensile properties. In this case, various parameters were used, including carbon content α (mass %), sample making process β (with $\beta = 1$ for CR, 2 for WQ, 3 for BH, and 4 for AN), and hydrogen charge γ (with $\gamma = 1$ for without hydrogen and 2 for with hydrogen). This analysis gave the following approximation equation:

$$\varepsilon_f = -16.63\alpha + 7.8\beta - 0.53\gamma \tag{2}$$

Figure 9 shows the relationship between the experimental tensile strengths (Fig. 5) and the values obtained from Eq. 2. It is clear that the multiple regression analysis results for CR and AN samples are in good agreement with the experimentally obtained fracture strain. On the other hand, the analyzed ε_f values for WQ and BH are slightly higher than that for their experimental strain value.

Hence, Eq. 2 can be modified to estimate their strain value depending on the sample treatment.

$$\varepsilon_f = x(-16.63\alpha + 7.8\beta - 0.53\gamma) \tag{3}$$

where x is the coefficient: $x = 1$ for CR and AN, 0.75 for WQ and 0.5 for BH. In the previous work [12], hydrogen embrittlement properties of high carbon steel were investigated: Fe-0.33C-1.2Mn-0.3Mo-0.005P-0.005S (in mass%), in which the experimental strain values for hydrogen charged CR and AN were obtained as follows, e.g., CR: 4% and AN: 22.5%, which is relatively similar to the numerical strain value, obtained with Eq. 3, e.g., CR: 1.24% and AN: 24.6%.

5 Conclusions

The hydrogen embrittlement characteristics of the low carbon steels with different microstructural characteristics, including different phase structures, precipitates, surface condition, and internal strain, were examined experimentally and numerically. The results can be summarized as follows:

1) High internal strain was obtained in CR, WQ, and BH, while the low strain was detected in AN. The high strain for CR was caused by the severe plastic deformation, through cold rolling process, and the high strain for WQ (and BH) was created by the martensite phase transformation through the quenching process. ε-carbide was precipitated similarly in the WQ and BH samples. The amount of ε-carbide was correlated with their carbon content.

2) HE occurred in the CR-0.15C and WQ-0.15C despite the low tensile strength of ~ 1200 MPa, in which HE was affected by the severe internal strain and high carbon content. On the other hand, weak HE was seen in

other samples even after the hydrogen charging was conducted. Different extent of HE was relatively related to the amount of diffusible hydrogen.

3) The surface treatments make high mechanical properties, where high amount of hydrogen is accumulated due to high internal strain. HE occurred severely in the shot-peened and nitrided CR-0.15C after the hydrogen charging, where the hydrogen trapping state at in high internal strain could be affected

4) For the hydrogen charged specimens, the tensile strain value decreased although the ultimate tensile strength was not altered. Numerical analysis was carried out to estimate successfully the extent of HE for the carbon steels via a multiple regression analysis.

Declarations

Conflict of interest The authors declare no conflict of interest.

References

1. Momotani Y, Shibata A, Daisuke Terada N, and Tsuji, *Int. J. Hydrogen Energy* **42** (2017) 3371.
2. Shibata A, Yonemura T, Momotani Y, Park M-H, Takagi S, Madi Y, Besson J, and Tsuji N, *Acta Mater.* **210** (2021) 116828
3. Nagao A, Hayashi K, Oi K, and Mitao S, *ISIJ Int.* **52** (2012) 213.
4. Okayasu M, and Fujiwara T, *Int. J. Hydrogen Energy* **46** (2021) 19657.
5. Dayal R K, and Parvathavarthini N, *Sâdhanâ* **28** (2003) 431.
6. Lee S-J, Ronevich J A, Krauss G, and Matlock D, *ISIJ Int.* **50** (2010) 294.
7. Barannikovaa S A, Kosinovc D A, Zueva L B, Gromovc V E, and Konovalov S V, *Steel in Translation* **46** (2016) 851.
8. Louthan M R Jr, *J. Fail. Anal. Preven.* **8** (2008) 289.
9. Chan S L I, and Charles J A, *Mater. Sci. Technol.* **2** (1986) 956.
10. Murakami Y, Kanezaki T, and Sofronis P, *Eng. Fract. Mech.* **97** (2013) 227.
11. Baker L J, Daniel S R, and Parker J D, *Mater. Sci. Tech.* **18** (2002) 355.
12. Okayasu M, Arai R, and Senuma T, *Int. J. Fract.* **231** (2021) 257.